Nano Research

Open Access

Research Article

CO adsorption, activation, and oxidation on CeO_2(111)-supported Fe model catalyst surfaces

Xingwang Cheng[1,§], Yi Tu[1,§], Dongling Zhang[1], Dong Han[1], Luchao Huang[1], Jun Hu[1], Honghe Ding[1], Qian Xu[1] ✉, and Junfa Zhu[1,2] ✉

[1] *National Synchrotron Radiation Laboratory, University of Science and Technology of China, Hefei 230029, China*
[2] *Department of Chemical Physics, Key Laboratory of Surface and Interface Chemistry and Energy Catalysis of Anhui Higher Education Institutes, and Key Laboratory of Precision and Intelligent Chemistry, University of Science and Technology of China, Hefei 230026, China*
[§] *Xingwang Cheng and Yi Tu contributed equally to this work.*

Cite this article: *Nano Research*, **2025**, *18*, 94907093. https://doi.org/10.26599/NR.2025.94907093

ABSTRACT: Elucidating the synergistic effect of Fe on CeO_2 is challenging in CO-related reactions but attractive owing to the improvement in the oxygen storage/release capacity of ceria with the addition of Fe. Here, using CeO_2(111)-supported Fe model catalysts, CO adsorption, activation, and oxidation on catalyst surfaces was carefully investigated using synchrotron radiation photoemission spectroscopy (SRPES), temperature-programmed desorption (TPD), and infrared reflection absorption spectroscopy (IRRAS). The precursor π-bonding state for CO dissociative adsorption has been identified through unusually low CO vibration frequencies and a low dissociation temperature on Fe/CeO_2(111) surfaces. CO is oxidized by dissociated atomic O followed by the Langmuir–Hinshelwood mechanism, whereas the lattice oxygen of CeO_2 exhibits low activity. The CO_2 yield displays a volcanic curve as a function of Fe coverage. On the 0.6 ML Fe/CeO_2 surface, weakly bound atomic O on Fe^{2+} results in the best catalytic activity. While on high Fe coverage surfaces, the CO_2 yield is limited due to the capture of atomic O by Fe^0. Our results provide comprehensive insights into the adsorption, activation, and oxidation of CO on Fe/CeO_2 and identify the reaction mechanism, and the active site, which provides deeper insights into CO-related reaction mechanisms over CeO_2-supported Fe catalysts.

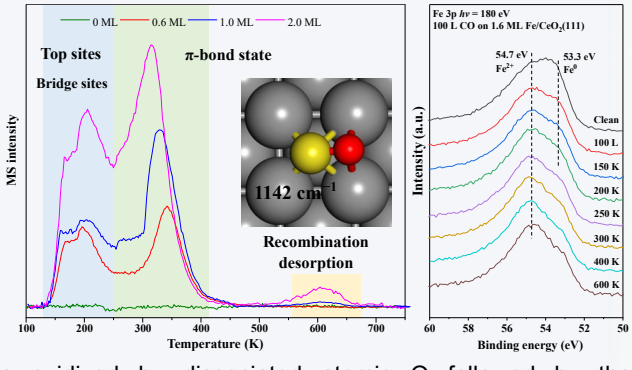

KEYWORDS: iron/ceria, model catalyst, adsorption, activation, oxidation

1 Introduction

Ceria (CeO_2), a key component of many heterogeneous catalyst systems, is widely used in many fields due to its redox property of oxygen storage and release (OSRC) [1]. However, the use of pure CeO_2 is limited by the low reactivity and degradation of OSRC over time [2]. Therefore, other metals, such as Pt [3], Pd [4], Fe [5], and Cu [6], are normally introduced into ceria to add catalytic active sites and improve the OSRC [1, 7]. Although the loading of some noble metals can reduce the reaction barrier by activating surface O, it is ineffective in increasing the total OSRC [1]. Transition-metal Fe, which is environmentally friendly and inexpensive, can significantly increase the OSRC of ceria, according to the measurements of Lambrou and Efstathiou [8]. Therefore, Fe-modified CeO_2 shows excellent catalytic performance in CO oxidation [9], selective catalytic reduction of NO_x [10], Fischer–Tropsch synthesis [11], and soot oxidation [12].

CO oxidation, as a model oxidation reaction, is also a key step in many catalytic reactions. Despite extensive research on CO oxidation reaction on the Fe/CeO_2 catalysts, the key fundamental issues related to the reaction mechanism and active sites remain unclear. For example, using isotopic labeling, Galvita et al. [13] reported that the initial reaction of CO and lattice O of ceria produced CO_2 through the Mars-van–Krevelen (MvK) mechanism. However, the experiments conducted by Li et al. [10] revealed that Fe:CeO_2 at different ratios displayed similar maximum combustion rate in catalytic coke combustion, indicating that the MvK

Received: September 29, 2024; **Revised:** October 16, 2024
Accepted: October 24, 2024

✉Address correspondence to Qian Xu, qianxu@ustc.edu.cn; Junfa Zhu, jfzhu@ustc.edu.cn

mechanism involving CeO_2 is improbable. Using density functional theory (DFT) calculations, Chen et al. [14] investigated the elementary reaction steps of CO oxidation on Fe supported on CeO_2 surface and found that the adsorbed CO was oxidized by a lattice O atom, following the MvK mechanism. However, the DFT theoretical calculation results of Tian et al. [15] reported that the loading of Fe increases the oxygen vacancy formation energy of CeO_2, thereby limiting the activity of lattice oxygen in the oxidation of CO via the MvK mechanism. Regarding the active sites of the CO oxidation on Fe/CeO_2 catalysts, Lykaki et al. [16] found that the CO conversion rate increased with increasing Fe^{2+} content in real Fe/CeO_2 catalyst, thus they believed that Fe^{2+} was the active site. Ge et al. [17] found that the catalytic activity decreased with Fe^{3+} content. Therefore, they concluded that Fe^{3+} was the active site, whereas Fe^{2+} merely played an auxiliary role in the catalysis by Fe^{3+} [17].

To resolve the abovementioned debates about the reaction mechanism and the nature of active sites for CO oxidation on Fe/CeO_2 at the atomic-molecular level, herein, we used "model catalysts" approach and constructed a simplified but well-defined experimental model system, $CeO_2(111)$ supported Fe nanoparticles, to investigate the CO adsorption, reaction, and oxidation. In our previous work, we systematically studied the morphological and electronic structures of ceria-supported Fe model catalysts [18]. At low coverage, charge transfer occurs between Fe and $CeO_2(111)$, leading to the formation of an Fe-O-Ce mixed oxide layer. Above 0.71 ML Fe coverage, metallic Fe^0 gradually increases and dominates. In the present study, based on the previous results, we prepared the $Fe/CeO_2(111)$ model catalysts first and then, using temperature-programmed desorption (TPD), *in situ* infrared reflection absorption spectroscopy (IRRAS), and synchrotron radiation photoemission spectroscopy (SRPES), the adsorption, activation, and oxidation of CO on $Fe/CeO_2(111)$ were systematically investigated. Our results clearly revealed the reaction mechanism and active sites for CO oxidation on the $Fe/CeO_2(111)$ model catalysts, providing the atomic-molecular level understanding for the long-term under debate issues.

2 Experimental section

The experiments were performed in three separate ultrahigh-vacuum (UHV) systems with base pressures below 1×10^{-10} mbar. The $Fe/CeO_2(111)$ model catalysts were prepared on Cu(111) by physical vapor deposition (PVD). The detailed procedure can be found in our previous paper [19]. Briefly, the Cu(111) surface was cleaned by repeated cycles of Ar^+ sputtering and annealing in UHV at 850 K until no contaminants were detected. Then, epitaxial $CeO_2(111)$ layer was grown onto the clean Cu(111) substrate by PVD of Ce (99.9999%, Alfa Aesar) metal in an oxygen atmosphere ($P = 5 \times 10^{-7}$ mbar) at 800 K, followed by annealing at 850 K for 10 min to achieve a better ordering. Fe was evaporated onto ceria films by direct PVD of Fe (99.99%, Alfa Aesar) at 300 K. According to our previous research [18], at low coverages (< 0.71 ML), the deposited Fe tended to grow randomly to form two-dimensional islands on $CeO_2(111)$. In addition, charge transfer occured from Fe to $CeO_2(111)$, leading to the formation of an Fe-O-Ce mixed oxide layer. Above 0.71 ML Fe coverage, three-dimensional Fe clusters formed, with metallic Fe^0 gradually increasing and becoming dominant. The TPD experiments were conducted in a separated UHV chamber with a base pressure below 1×10^{-10} mbar. This chamber was equipped with a sputtering gun, an Auger spectrometer, a differential-pumped Hiden mass spectrometer for TPD, and a sample manipulator with resistive heating where the single-crystal sample was held by two Ta wires. The sample temperature was measured by a K-type thermocouple that was directly attached to the side of the sample. The isotope gas $^{13}C^{16}O$ was used to avoid background gas contamination. To distinguish O from the dissociative adsorption $^{13}C^{16}O$ and lattice O of CeO_2, $Ce^{18}O_2(111)$ films were grown using the isotope gas $^{18}O_2$. Before $^{13}C^{16}O$ was dosed, possible traces of volatile carbonyls were purified using a liquid nitrogen cooling trap. For the CO-TPD experiments, the Fe/CeO_2 model catalysts were exposed to 100 L of $^{13}C^{16}O$ at 100 K, followed by programmed heating to 800 K at a rate of 2 K/s.

IRRAS experiments were performed at the photoemission endstation at the BL10M beamline in the National Synchrotron Radiation Laboratory (NSRL), which has three UHV chambers, i.e., the analysis chamber, the preparation chamber, and the IRRAS chamber, with base pressures in the 10^{-10} mbar range, which has been described previously [20]. The samples were first cleaned and prepared in the preparation chamber. Then, they were characterized with SRPES in the analysis chamber. IRRAS experiments were subsequently performed in the IR chamber. Before the CO dosing, a background spectrum of the clean sample was recorded (spectral resolution: 4 cm^{-1}, acquisition time: 10 min), after which a blank infrared spectrum was acquired (acquisition time: 1 min). Subsequently, the sample was exposed to CO ($P_{CO} = 1 \times 10^{-8}$ mbar), and the IR spectra were recorded every minute in the "collecting series" mode.

The SRPES measurements were performed at the Catalysis and Surface Science Endstation in the NSRL, which has four UHV chambers with base pressures below 10^{-10} mbar, as described in detail elsewhere [19, 21]. After the model catalysts were prepared in the preparation chamber, they were transferred to the analysis chamber for the SRPES measurements. The photon energy was set at 380 eV for C 1s and 180 eV for Fe 3p. The sample was exposed to 100 L of CO at 100 K, followed by step heating to 600 K. The Fe 3p and C 1s spectra were collected after each annealing.

3 Results and discussion

To investigate the CO desorption state on the $Fe/CeO_2(111)$ model catalysts with different Fe coverages, we first performed TPD experiments by exposing the surface to 100 L of $^{13}C^{16}O$ at 100 K followed by programmed heating (2 K/s) and monitoring the desorption of gases from the surface using a mass spectrometer. The TPD spectra for $^{13}C^{16}O$ (mass 29), $^{13}C^{16}O_2$ (mass 45), $^{13}C^{16}O^{18}O$ (mass 47), and $^{13}C^{18}O_2$ (mass 49) for $^{13}C^{16}O$ adsorption on $Fe/CeO_2(111)$ with different Fe coverages are shown in Fig. S1 in the Electronic Supplementary Material (ESM). Figure 1 shows the TPD spectra for $^{13}C^{16}O$ (mass 29). As seen, no CO desorption peak after 100 L $^{13}C^{16}O$ adsorption on the pure $CeO_2(111)$ surface at 100 K is observed (the green line in Fig. 1), in agreement with previous studies [22]. On $Fe/CeO_2(111)$ with low Fe coverage of 0.6–1.0 ML, two broad desorption peaks of $^{13}C^{16}O$ appear at approximately 200 and 320 K, with a shoulder peak at ~ 160 K; these peaks intensify with increasing Fe coverage. When Fe coverage is higher than 1.0 ML, a new desorption peak of $^{13}C^{16}O$ is observed at ~ 600 K. In general, these desorption features are very similar to those observed on the low-index planes of Fe [23, 24], where the desorption peaks around 200 K with the shoulder peak at ~ 160 K were assigned to the desorption of CO adsorbed on the top and bridge sites, respectively, while the desorption peak around

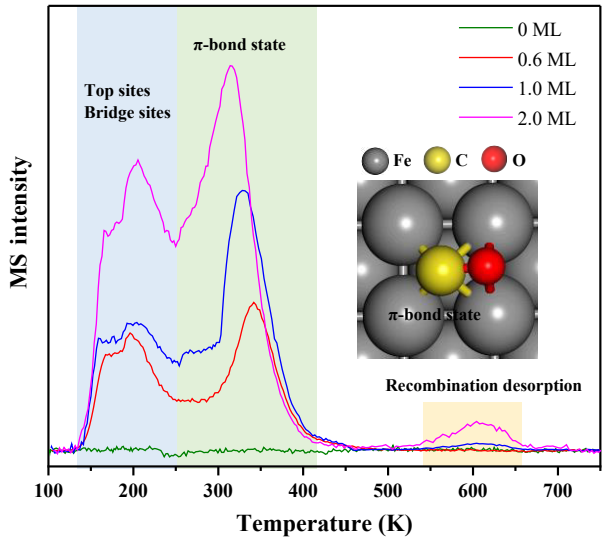

Figure 1 Series of TPD spectra of 100 L $^{13}C^{16}O$ adsorption on Fe/CeO_2(111) at 100 K with different Fe coverages.

~ 320 K was attributed to the desorption of CO molecules coordinated to the low-index planes of Fe surface via both the carbon and oxygen ends of the molecule which was referred as a π-bonded geometry [25, 26]. Therefore, we follow the similar assignments for the desorption peaks below 400 K shown in Fig. 1. It should be noted that the π-bonded CO state observed at low temperatures exclusively underwent dissociation upon heating at low CO exposures [27–29], while at higher CO coverages, both dissociation and desorption occurred [29, 30]. However, on the surface of CeO_2(111)-supported Fe, one may argue that the interatomic distances between Fe atoms should differ from those of the low-index planes of iron, which makes it difficult for the C–O bond length to match the interatomic distances of Fe in the π-bonded CO state. Indeed, from our previous study, we know that when the Fe coverage below 0.71 ML, Fe^{2+} forms in the configuration of Fe-O-Ce [18]. The repulsion between Fe atoms resulted in the lattice constant of the ideal Fe-O-Ce wetting layer to be 4.4 Å [18]. According to the report from Li [26] and Lu et al. [30], the π-bonded CO adsorption configuration only required a C–O bond length to be less than half of the interatomic distance of the Fe atoms. In addition, the weakening of the C–O bond also resulted in the elongation of the C–O bond length. Therefore, the π-bonded CO adsorption state on the Fe-O-Ce surfaces in the present case is feasible since the 100 L CO exposure almost saturates the Fe/CeO_2(111) at 100 K. The structure model is shown in the inset of Fig. 1. In addition, the desorption peak around 600 K appeared at Fe coverage higher than 1 ML can be attributed to the recombination of dissociated CO [29, 31]. The disappearance of this peak at coverages below 1 ML of Fe will be discussed in the next section.

Figure 2 shows the IRRA spectra of 90 L of CO adsorbed on the 0.6 ML and 1.6 ML Fe/CeO_2(111) surfaces at 100 K and then heated to 300 K. On the 0.6 ML Fe/CeO_2(111) surface (Fig. 2(a)), characteristic absorption bands at 2173, 2121, 2069, 1987, 1458, 1260, and 1180 cm^{-1} can be observed. The bands at 2173 cm^{-1} can be assigned to the stretching frequencies of CO adsorbed on Ce^{3+} centers. The bands at 1458 and 1260 cm^{-1} can be assigned to monodentate carbonate (m-CO_3^{2-}) and carboxyl ($CO_2^{\delta-}$) species, respectively [32, 33], which are also observed by SRPES (see next section). Based on the CO vibration frequencies reported for the low-index planes of Fe and the supported Fe catalysts (Table S1 in the ESM), the CO bands at 2121, 2069, 1987, and 1180 cm^{-1} can be assigned to the stretching frequencies of CO adsorbed on Fe^{2+} (0.6 ML Fe on CeO_2) at the top, bridge and 3-fold hollow sites, and π-bond state, respectively [34–37]. The 3-fold hollow state does not appear separately in TPD (Fig. 1), which may be due to its overlap with other desorption peaks. Upon stepwise heating of the surface to 200 K (Fig. 2(b)), the CO bands at 2173, 2121, 2069, and 1987 cm^{-1} and the bands for the m-CO_3^{2-} and $CO_2^{\delta-}$ species at 1458 and 1260 cm^{-1} disappeared. This is consistent with the desorption temperatures of CO adsorbed on top, bridge and 3-fold hollow sites in TPD (Fig. 1), which are below 200 K. After further heating to 300 K (Fig. 2(b)), only the CO band at 1180 cm^{-1} remains visible on the surface. This is also consistent with the desorption temperature of π-bond state CO in TPD, which is above 300 K.

Figure 2(c) shows a series of IRRA spectra observed after exposure of 1.6 ML Fe/CeO_2(111) to different doses of CO at 100 K. After exposing the surface to 0.18 L of CO at 100 K, we also observed CO bands at 2121 and 2069 cm^{-1} for CO on top and bridge sites (both on Fe^{2+}), respectively. In addition, new CO bands appear at 1990, 1958, 1888, 1740, and 1142 cm^{-1}. With increasing CO exposure, the following changes in the spectra are observed: (1) all the vibrational peaks gain intensity; (2) the band at 1990 cm^{-1} also increases in intensity with CO exposure and it shifts to 2038 cm^{-1}. This shift typically results from the dipole coupling of CO adsorbed on metals [38]; (3) the bands for the m-CO_3^{2-} and $CO_2^{\delta-}$ species also appear at 1458 and 1260 cm^{-1}. According to the Ref. [39], the frequencies of the CO bands for molecularly adsorbed CO on the metallic Fe^0 were approximately 100 cm^{-1} lower than for molecularly adsorbed CO on Fe^{2+} [40]. From our previous study, we know that when the Fe coverage reaches 1.6 ML, the metallic Fe^0 dominates [18]. Therefore, we assigned the CO bands at 2038, 1958, and 1888 cm^{-1} to CO adsorbed on Fe^0 (1.6 ML Fe on CeO_2) at the top, bridge, and 3-fold hollow sites, respectively. It should be mentioned that this CO adsorbed on 3-fold hollow sites do not appear separately in TPD (Fig. 1), which may be due to its overlap with other desorption peaks. The 1142 cm^{-1} band is attributed to the π-bond state of CO on Fe^0 (see detailed discussion in next section), and the 1740 cm^{-1} band is attributed to the bridged carbonate (b-CO_3^{2-}) on the Fe/CeO_2 surface [33]. This band can only be observed at high Fe coverages on CeO_2. This observation is consistent with previous studies that the bridged carbonate becomes more evident at higher Fe:Ce ratios in FeO-CeO_2 catalysts, where Fe^0 and Fe^{2+} coexist [41]. After stepwise heating the surface to 300 K (Fig. 2(d)), the CO band at 1888 cm^{-1} decreases in intensity and disappears completely at 160 K. The intensity of the π-bond state of CO on Fe^0 at 1142 cm^{-1} and the b-CO_3^{2-} at 1740 cm^{-1} decreases. In addition, the bands attributed to CO on top sites of Fe^0 redshift to 2026 cm^{-1}. Compared to the TPD results (Fig. 1), some CO adsorbed on top and bridge sites at 2026–1958 cm^{-1} remain visible on the 1.6 ML Fe/CeO_2 surface.

The π-bonded CO state requires a large electronic donation to the antibonding CO 2π* orbitals [29, 42]. Thus, in this study, the CO stretching vibration frequency on the Fe^{2+} surface is unusually low at 1180 cm^{-1} [42]. The increase in the d-band electron density of metallic Fe at the 1.6 ML Fe/CeO_2(111) surface enables greater electron backdonation to the antibonding CO 2π* orbitals, which results in further weakening of the C–O bond and a shift in the stretching vibration frequency of the π-bonded CO state from 1180 cm^{-1} on the Fe^{2+} surface to 1142 cm^{-1} on the Fe^0 surface. In summary, for Fe on CeO_2(111) with coverages lower than 0.71 ML,

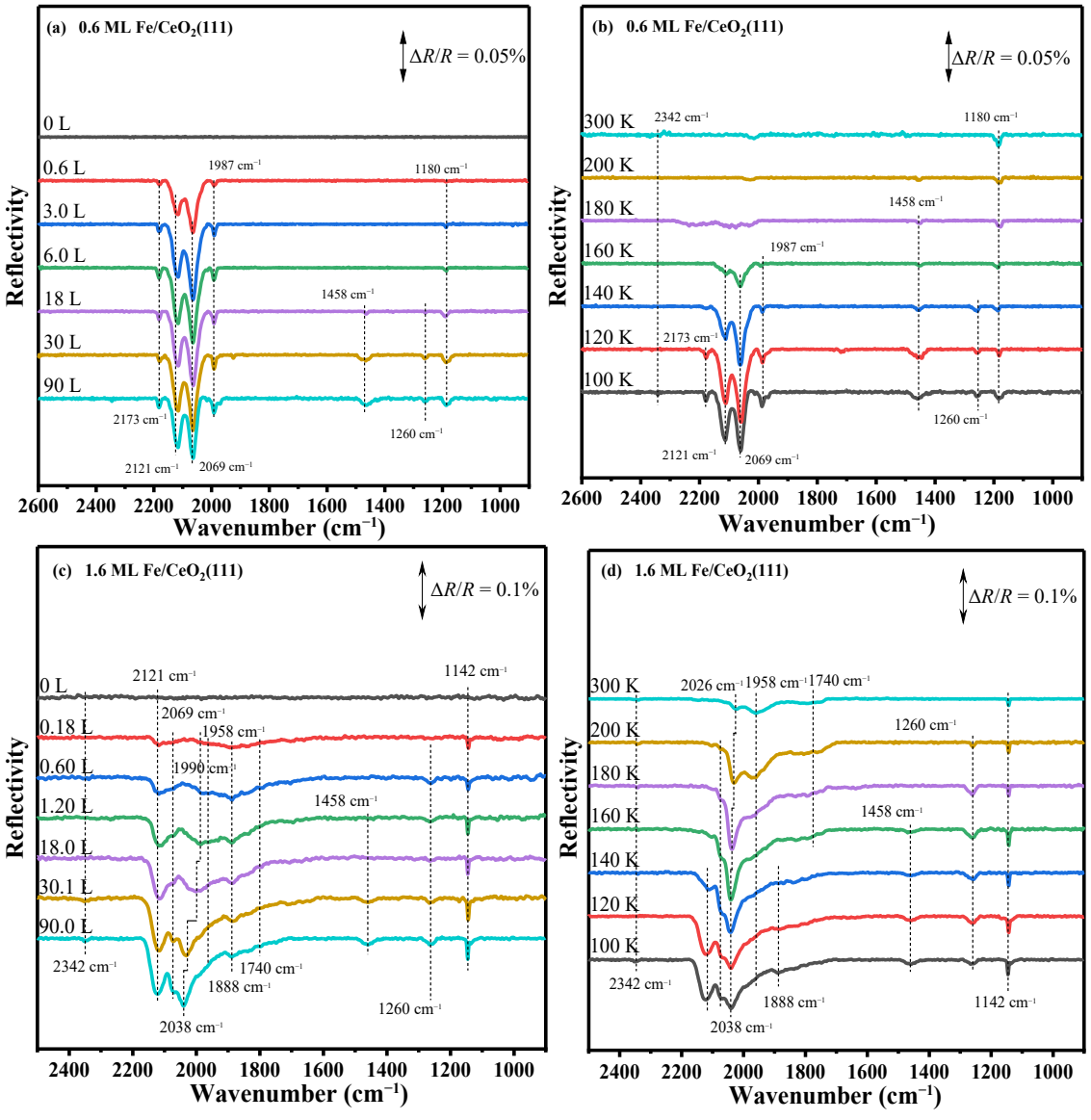

Figure 2 IRRA spectra obtained from the 0.6 ML Fe/CeO_2 surface with incremental doses of CO at 100 K (a), followed by heating to different temperatures (b). IRRA spectra obtained from the 1.6 ML Fe/CeO_2 surface with incremental doses of CO at 100 K (c), followed by heating to different temperatures (d).

Fe^{2+} dominates the surface. CO molecules coordinated to Fe^{2+} as a π-bonded geometry. This configuration results in a weaker C–O bond and a lower CO stretching vibration frequency. Above 0.71 ML, metallic Fe^0 gradually increases and dominates. CO molecules coordinated to the Fe^0 surface also as a π-bonded geometry. This configuration on Fe^0 is characterized by an even weaker C–O bond, resulting in a further decreased CO stretching vibration frequency. As the π-bonded CO adsorption configuration is considered to be a precursor for CO dissociation, the emergence of Fe^0 with increasing Fe coverage is more beneficial to CO dissociative adsorption.

To investigate the reaction pathways and active sites of CO oxidation on $Fe/CeO_2(111)$ surfaces, we used $^{18}O_2$ gas to grow $Ce^{18}O_2(111)$ and subsequently performed TPD experiments with 100 L of $^{13}C^{16}O$ adsorbed on the 0.6 ML and 2.0 ML Fe/CeO_2 surfaces. For the CO_2 production, we monitored three kinds of CO_2, i.e., $^{13}C^{16}O_2$ (mass 45), $^{13}C^{16}O^{18}O$ (mass 47), and $^{13}C^{18}O_2$ (mass 49), to investigate the role of lattice oxygen of $CeO_2(111)$ in CO oxidation. Figure 3(a) shows the TPD results of CO_2 on the 0.6 ML Fe/CeO_2 surface. As can be seen, the main product is $^{13}C^{16}O_2$ with the desorption temperature of approximately 400 K. In addition, a small amount of $^{13}C^{16}O^{18}O$ is also observed. Almost no $^{13}C^{18}O_2$ product, which results from the oxidation of atomic ^{13}C by two lattice ^{18}O of $Ce^{18}O_2$, is detected. Notably, the $^{13}C^{16}O^{18}O$ product should originate from the oxidation of $^{13}C^{16}O$ by lattice ^{18}O ($Ce^{18}O_2$), following the MvK mechanism. In this mechanism, CO reacts directly with lattice oxygen to produce CO_2 [43]. On the other hand, the $^{13}C^{16}O_2$ product is formed from the oxidation of $^{13}C^{16}O$ by atomic ^{16}O from $^{13}C^{16}O$ dissociation. This reaction may follow the Langmuir–Hinshelwood (LH) mechanism, where adsorbed CO reacts with an adsorbed atomic ^{16}O from $^{13}C^{16}O$ dissociation [43].

Figure 3(b) shows the TPD results of CO_2 following the adsorption of 100 L of $^{13}C^{16}O$ on the 2.0 ML Fe/CeO_2 surface at 100 K. Similar to those on the 0.6 ML Fe/CeO_2 surface, the main reaction product is again $^{13}C^{16}O_2$ with a small amount of $^{13}C^{16}O^{18}O$, and the desorption peak is about 450 K. The desorption temperature of $^{13}C^{16}O_2$ is higher on 2.0 ML Fe/CeO_2 (450 K) than on 0.6 ML Fe/CeO_2 (410 K). This discrepancy will be discussed in the next section. Different from those on 0.6 ML Fe/CeO_2, the

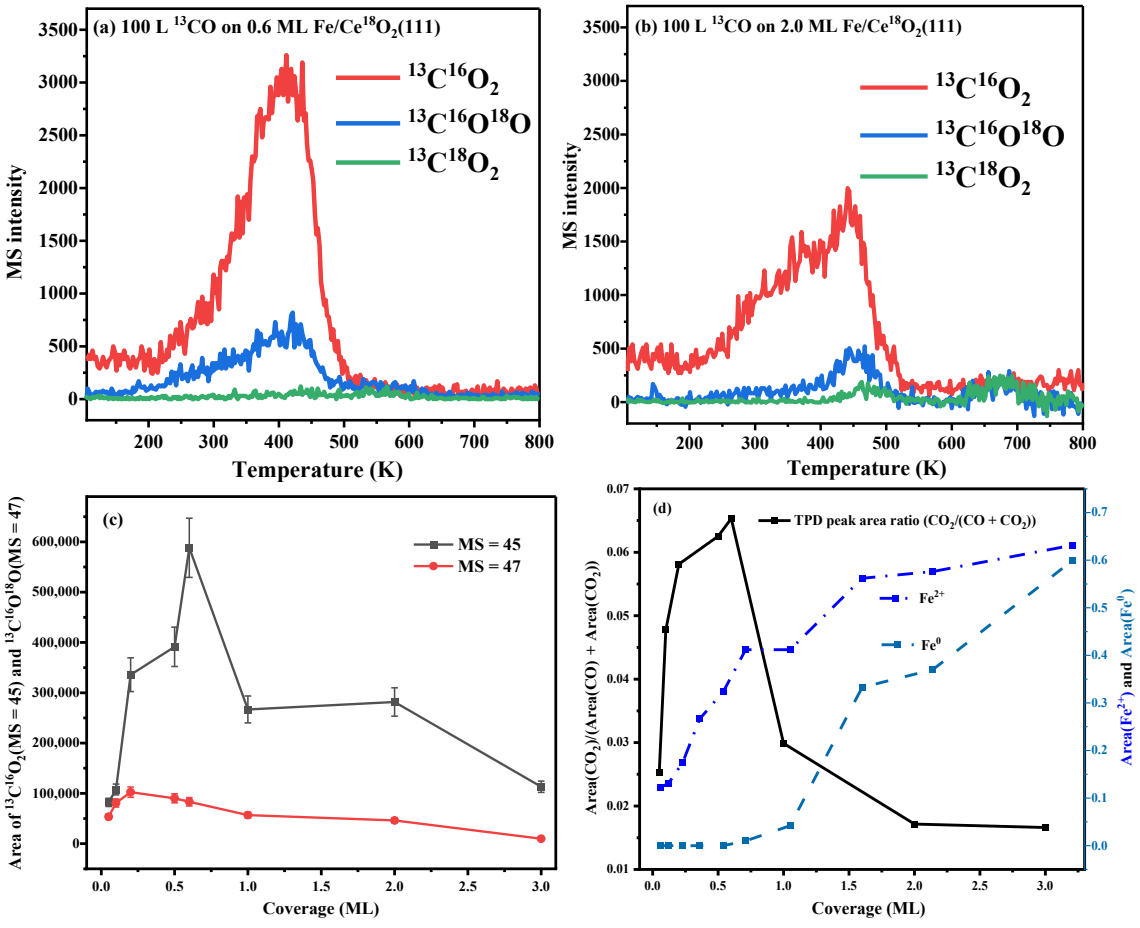

Figure 3 TPD spectra for $^{13}C^{16}O_2$, $^{13}C^{16}O^{18}O$, and $^{13}C^{18}O_2$ obtained from 100 L $^{13}C^{16}O$ exposed to (a) 0.6 ML Fe/CeO_2(111) and (b) 2.0 ML Fe/CeO_2(111) at 100 K. (c) MS intensities of $^{13}C^{16}O_2$ (mass 45) and $^{13}C^{16}O^{18}O$ (mass 47) obtained from the TPD spectra on the Fe/CeO_2(111) surfaces as functions of Fe coverage. (d) MS intensity ratio of $^{13}C^{16}O_2$ (mass 45) + $^{13}C^{16}O^{18}O$ (mass 47) to $^{13}C^{16}O$ (mass 29) + $^{13}C^{16}O_2$ (mass 45) + $^{13}C^{16}O^{18}O$ (mass 47) obtained from the TPD spectra and XPS peak intensities of Fe^{2+} and Fe^0 on the Fe/CeO_2(111) surfaces as functions of the Fe coverage. These XPS intensities are derived from the fitting of Fe 2p spectra for different amounts of Fe deposited on the CeO_2(111) surface at 300 K, as illustrated in Fig. S2 in the ESM.

$^{13}C^{16}O_2$ and $^{13}C^{16}O^{18}O$ desorption intensities decreases on the 2.0 ML Fe/CeO_2 surface, and, moreover, new weak desorption peaks for $^{13}C^{16}O^{18}O$ and $^{13}C^{18}O_2$ appear at 600 K. These new weak desorption features likely arise from the oxidation of $^{13}C^{16}O$ and atomic ^{13}C by lattice ^{18}O reverse spillover of $Ce^{18}O_2$. This phenomenon has also been observed in Rh/CeO_2 [44].

To clarify the relationship between Fe coverage and the CO oxidation mechanism on Fe/CeO_2 surfaces, we plot the desorption intensities of $^{13}C^{16}O_2$ (mass 45) and $^{13}C^{16}O^{18}O$ (mass 47) from TPD results after heating 100 L of $^{13}C^{16}O$ adsorbed on the 0.6 ML and 2.0 ML Fe/CeO_2 surfaces, as a function of Fe coverage. The results are shown in Fig. 3(c). With increasing Fe coverage, the desorption intensity of $^{13}C^{16}O_2$ increases significantly and reaches its maximum value at 0.6 ML Fe coverage. As the Fe coverage increases further, the desorption intensity of $^{13}C^{16}O_2$ sharply decreases. In contrast, the desorption intensity of $^{13}C^{16}O^{18}O$ exhibits a slight increase up to 0.3 ML Fe coverage, after which it decreases to a low value with further increases in Fe coverage.

It is evident that $^{13}C^{16}O_2$ is the main product on Fe/CeO_2(111) with Fe coverage of 0–3.0 ML. Therefore, it can be concluded that CO oxidation on Fe/CeO_2 surfaces mainly proceeds via the LH mechanism. The same phenomenon is also observed for CO adsorption on Fe supported on thin-film silica [45]. On the Fe/SiO_2 surface, the O species generated from CO dissociation on the Fe species remain stable until they react with CO to form CO_2 at 150 °C. It should be noted that the Boudouard reaction [46], also known as CO disproportionation (2CO → CO_2 + C), produces a mass of 45 for $^{13}C^{16}O_2$ when using the isotope $^{13}C^{16}O$. However, because the Boudouard reaction temperature in Fe-containing catalysts typically exceeds 600 K, $^{13}C^{16}O_2$ produced from this reaction is negligible in this work. In addition, the decomposition of $CO_2^{\delta-}$ and CO_3^{2-} may also produce a mass of 45 for $^{13}C^{16}O_2$. However, after the decomposition of CO_3^{2-} and $CO_2^{\delta-}$, no discernible CO_2 signal is observed, which should appear at 2342 cm^{-1} in IRRAS and below 300 K in TPD on both 0.6 ML and 2.0 ML Fe/CeO_2(111) surfaces.

To further elucidate the relationship between CO oxidation and Fe coverage on Fe/CeO_2 surface, the correlation of the TPD (Fig. S1 in the ESM) and Fe 2p XPS (Fig. S2 in the ESM) results is analyzed. The results are shown in Fig. 3(d). Specifically, the MS intensity ratio of $^{13}C^{16}O_2$ (mass 45) + $^{13}C^{16}O^{18}O$ (mass 47) to $^{13}C^{16}O$ (mass 29) + $^{13}C^{16}O_2$ (mass 45) + $^{13}C^{16}O^{18}O$ (mass 47), also known as $^{13}C^{16}O_2$ yield, is attained from the TPD spectra (Fig. S1 in the ESM). The XPS peak intensities of Fe^{2+} and Fe^0 species on the Fe/CeO_2(111) surfaces are obtained from the fitting of Fe 2p spectra for different amounts of Fe deposited on the CeO_2(111) substrate, as illustrated in Fig. S2 in the ESM [47–49]. As seen in Fig. 3(d), with increasing Fe coverage to 0.6 ML, the peak intensity of Fe^{2+} increases

accompanied by a rapid increase in $^{13}C^{16}O_2$ yield. When the Fe coverage exceeds 0.6 ML, the peak intensity of metallic Fe^0 increases, while the $^{13}C^{16}O_2$ yield dramatically decrease. In summary, the reactivity of Fe/CeO_2 surfaces towards CO oxidation is highly dependent on the Fe coverage. At low Fe coverage on CeO_2 surface, the Fe^{2+} significantly promotes the oxidation of $^{13}C^{16}O$ to $^{13}C^{16}O_2$. Conversely, at high Fe coverage, the appearance of Fe^0 inhibits the oxidation process. Thus, it can be concluded that Fe^{2+} on Fe/CeO_2 surfaces serves as the active site for CO oxidation.

To better understand the nature of the reaction mechanism and active site of CO oxidation on Fe/CeO_2, we performed SRPES experiments with 100 L of CO adsorbed on 0.6 ML and 1.6 ML Fe/CeO_2 surfaces at 100 K and subsequently heated to 600 K. The collected C 1s and Fe 3p spectra are shown in Fig. 4. On the 0.6 ML Fe/CeO_2 surface, after exposure to 100 L of CO at 100 K, four peaks appear in the C 1s spectrum at binding energies (BEs) of 284.5, 285.4, 288.4, and 289.6 eV (Fig. 4(a)), which can be attributed to atomic C, molecularly adsorbed CO, $CO_2^{\delta-}$, and CO_3^{2-}, respectively [32, 50, 51]. To better observe them, we carefully fitted the C 1s peaks of these species. As the temperature increases up to 250 K,

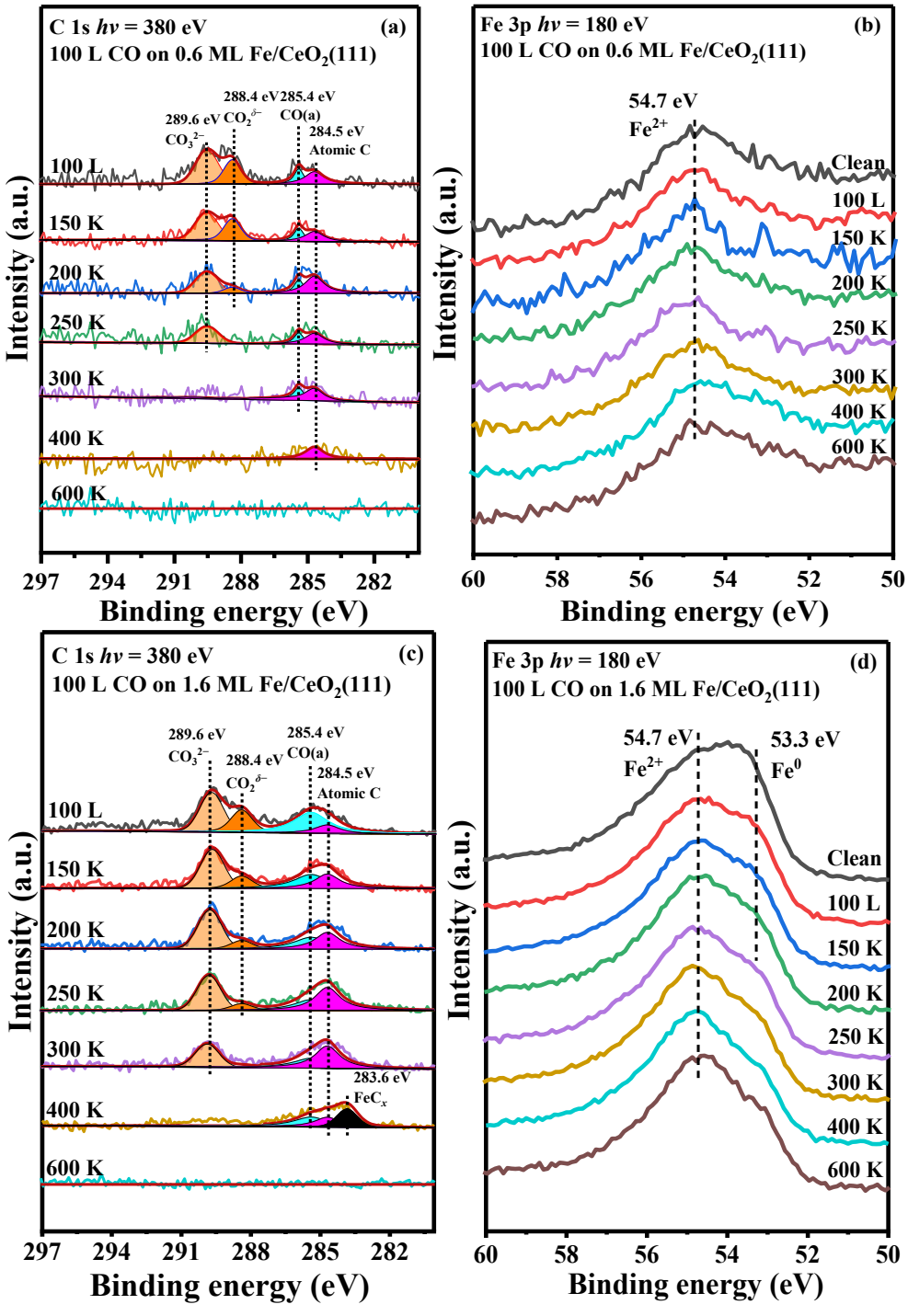

Figure 4 SRPE spectra of the 100 L of CO adsorbed on the 0.6 ML $Fe/CeO_2(111)$ surface: (a) C 1s ($h\nu$ = 380 eV) and (b) Fe 3p ($h\nu$ = 180 eV), and on the 1.6 ML $Fe/CeO_2(111)$ surface: (c) C 1s ($h\nu$ = 380 eV) and (d) Fe 3p ($h\nu$ = 180 eV), at 100 K followed by heating to different temperatures.

the signals for the molecularly adsorbed CO, $CO_2^{\delta-}$, and CO_3^{2-} species gradually decrease. At 300 K, the signals for $CO_2^{\delta-}$ and CO_3^{2-} vanish, while the signals for the molecularly adsorbed CO and atomic C remain visible. At 400 K, the molecularly adsorbed CO is completely desorbed, and the amount of atomic C species decreases. When the temperature further increases to 600 K, the atomic C species disappears entirely. It is worth mentioning that, after exposing the 0.6 ML Fe/CeO_2 surface to 100 L of CO at 100 K, the presence of atomic C in C 1s spectrum confirms the dissociative adsorption of CO on this surface at low temperature. The Fe 3p spectra for the 0.6 ML Fe/CeO_2 surface exposed to 100 L of CO at 100 K are shown in Fig. 4(b). Before CO adsorption, a broad single peak emerges at BE of 54.7 eV. According to our previous research, this peak could be assigned to Fe^{2+} [18]. Upon CO adsorption at 100 K and subsequent annealing of the surface to 600 K, this peak exhibits no significant change in the BE.

Similarly, after exposing the 1.6 ML Fe/CeO_2 surface to 100 L of CO at 100 K, four peaks appear in the C 1s spectrum (Fig. 4(c)) at BEs of 284.5, 285.4, 288.4, and 289.6 eV. These peaks can be also attributed to atomic C, molecularly adsorbed CO, $CO_2^{\delta-}$, and CO_3^{2-}, respectively [32, 50, 51]. The fitting parameters for atomic C, CO_3^{2-}, and $CO_2^{\delta-}$ species are consistent with those of the same species in Fig. 4(a). However, the fitting parameters for the molecularly adsorbed CO species differ from those of the same species in Fig. 4(a). This variation may arise from the significant impact of different electronic states of Fe on the binding energy of C 1s in CO adsorption [50, 52], as shown in Fig. S2 in the ESM. Upon annealing the surface to temperatures of 150, 200, 250, and 300 K, the signals corresponding to molecularly adsorbed CO, $CO_2^{\delta-}$, and CO_3^{2-} gradually decrease in intensity, while the signal for atomic C intensifies. At 400 K, the signals for $CO_2^{\delta-}$ and CO_3^{2-} disappear, and a new peak is observed at a BE of 283.6 eV, which is attributed to the FeC_x species [53]. When the temperature further increases to 600 K, no peaks can be observed in C 1s spectrum. In contrast, the Fe 3p spectra for the 1.6 ML Fe/CeO_2 surface exposed to 100 L of CO at 100 K are shown in Fig. 4(d). Before CO adsorption, two broad peaks are observed at BE of 54.7 and 53.3 eV, corresponding to the Fe^{2+} and Fe^0 states (dominating), respectively [18]. Upon exposure to 100 L of CO at 100 K, the peak intensity of Fe^{2+} increases at the expense of that of the metallic Fe^0. Upon stepwise annealing the surface to temperatures of 150, 200, 250, and 300 K, the intensity of Fe^{2+} gradually increases, while the intensity of Fe^0 gradually decreases. By 400 K, Fe^{2+} becomes the dominant surface species, while Fe^0 almost disappears. Notably, the concentration of FeC_x species in this work is very low, and the Fe 3p spectrum generally has a large full width at half maximum (FWHM), making it difficult to unambiguously distinguish the FeC_x and Fe^0 species. In addition, the binding energy of FeC_x in the Fe 2p spectrum is located between that of Fe^0 and Fe^{2+} [53], making it also difficult to unambiguously distinguish the FeC_x and Fe^0 species. Therefore, the identification of FeC_x species in our work can be only based on the peak at 283.6 eV in the C 1s spectrum. When the temperature is further increased to 600 K, Fe^{2+} remains the dominant surface species, while the intensity of Fe^0 slightly increases.

Notably, after the 1.6 ML Fe/CeO_2 surface exposed 100 L CO at 100 K, the increase in Fe^{2+} intensity and decrease in Fe^0 intensity in the Fe 3p spectrum indicate the oxidation of Fe^0 during CO dissociation. The same phenomenon was also observed for CO adsorption on polycrystalline Fe foils [54]. The oxidation of Fe^0 after CO adsorption on 1.6 ML Fe/CeO_2 surface at 100 K demonstrates the capture of atomic O (dissociated CO) by metallic Fe^0. The binding of atomic O and Fe renders the trapped O inert, thereby reducing CO_2 yield. The increased binding strength requires a higher temperature for CO oxidation by atomic O to form CO_2, as shown in Figs. 3(a) and 3(b). Moreover, the trapped atomic O can recombine with atomic C and desorb only upon reaching 600 K, as shown in Fig. 3. In contrast, on 0.6 ML Fe/CeO_2 surface, the weakly bound atomic O (dissociated CO) exhibits high activity in oxidizing adsorbed CO to CO_2 at temperature below 500 K. This weakly bound atomic O also undergoes recombination with atomic C at temperatures below 450 K, as evidenced by the disappearance of atomic C in C 1s spectrum (Fig. 4(a)). In other words, the trapped O on the 1.6 ML Fe/CeO_2 surface was at a disadvantage in oxidizing CO and recombining with atomic C, which results in a lower CO_2 yield and a higher CO recombination desorption temperature than that on 0.6 ML Fe/CeO_2 surface. In Fig. 3(d), as the Fe coverage increases up to 0.6 ML, only the Fe^{2+} species is formed on the surface, and its concentration increases with the increase in Fe coverage. Correspondingly, the concentration of weakly bound oxygen on the Fe^{2+} surface also increases upon CO adsorption, leading to a gradual increase in CO_2 yield. However, when the Fe coverage reaches 0.71 ML, Fe^0 emerges and dominates. The binding of atomic O and Fe^0 renders the trapped O inert, thereby reducing CO_2 yield.

4 Conclusions

In this study, we prepared Fe/CeO_2(111) model catalysts by depositing different amounts of Fe on the thin CeO_2(111) film surface. CO adsorption, activation, and oxidation on the model catalysts are systematically studied using TPD, IRRAS, and SRPES.

For a low Fe coverage of 0.1–1.0 ML on the CeO_2(111) surface, Fe^{2+} dominates the surface. At low temperatures, CO is adsorbed on the Fe/CeO_2 surface in top, bridge sites, and π-bond state on the Fe^{2+} sites. For a high Fe coverage above 1.0 ML, metallic Fe^0 emerges and gradually dominates the surface. The adsorption states of CO in top, bridge sites, and π-bond state are like those observed on Fe^{2+} surfaces. However, a new desorption feature appears at approximately 600 K because of the recombination of atomic C and atomic O (dissociated CO).

CO molecules can dissociate on Fe/CeO_2 surfaces at 100 K, leading to the formation of atomic C and atomic O. On the 0.6 ML Fe/CeO_2 surface, these atomic species can recombine to form CO, which subsequently desorbs at temperature below 450 K. However, on the 2.0 ML Fe/CeO_2 surface, the recombination and desorption of CO occur at higher temperature (600 K).

On Fe/CeO_2 surface, CO is oxidized by atomic O from dissociated CO, following the LH mechanism. In contrast, the lattice O of CeO_2 has low activity in the CO oxidation. On the 0.6 ML Fe/CeO_2 (Fe^{2+} dominate) surface, the weakly bound atomic O and Fe^{2+} result in high catalytic activity of CO oxidation. While on the 1.6 ML Fe/CeO_2 (Fe^0 dominate) surface, the atomic O is trapped by Fe^0, resulting in a lower CO oxidation performance.

Electronic Supplementary Material: Supplementary material (TPD spectra obtained from 0.1–2.0 ML Fe on CeO_2(111) exposed to 100 L $^{13}C^{16}O$ at 100 K; Fe 2p spectra ($h\nu$ = 1253.6 eV) for different amounts of Fe deposited on the CeO_2(111) surface at 300 K and Fe $2p_{3/2}$ spectra of 1.6 ML Fe on CeO_2(111); CO stretching frequencies on the Fe single crystal and the oxide-supported Fe nanoparticles;

peak position, FWHM, and normalized peak area of Fe $2p_{3/2}$ from 1.60 ML Fe/CeO_2(111)) is available in the online version of this article at https://doi.org/10.26599/NR.2025.94907093.

Data availability

All data needed to support the conclusions in the paper are presented in the manuscript and the Electronic Supplementary Material. Additional data related to this paper may be requested from the corresponding author upon request.

Acknowledgements

This work was financially supported by the National Key R&D Program of China (No. 2023YFA1509103) and the National Natural Science Foundation of China (Nos. 22272157, 21872131, 22106085, and U1932214).

Declaration of competing interest

All the contributing authors report no conflict of interests in this work.

Author contribution statement

X. W. C. performed the experiments, conducted the data analysis, and wrote the first draft manuscript. J. F. Z. initiated the research, guided the data analysis and paper writing, reviewed and modified the paper. Q. X. co-performed the experiments, helped the data analysis and paper writing. Y. T., D. L. Z., and L. C. H. helped performing experiments. The manuscript was written through contributions of all authors. All authors have given approval to the final version of the manuscript.

Use of AI statement

None.

References

[1] Li, P.; Chen, X. Y.; Li, Y. D.; Schwank, J. W. A review on oxygen storage capacity of CeO_2-based materials: Influence factors, measurement techniques, and applications in reactions related to catalytic automotive emissions control. *Catal. Today* **2019**, *327*, 90–115.

[2] van Deelen, T. W.; Hernández Mejía, C.; de Jong, K. P. Control of metal-support interactions in heterogeneous catalysts to enhance activity and selectivity. *Nat. Catal.* **2019**, *2*, 955–970.

[3] Zhang, F.; Gutiérrez, R. A.; Lustemberg, P. G.; Liu, Z. Y.; Rui, N.; Wu, T. P.; Ramírez, P. J.; Xu, W. Q.; Idriss, H.; Ganduglia-Pirovano, M. V. et al. Metal-support interactions and C1 chemistry: Transforming Pt-CeO_2 into a highly active and stable catalyst for the conversion of carbon dioxide and methane. *ACS Catal.* **2021**, *11*, 1613–1623.

[4] Muravev, V.; Spezzati, G.; Su, Y. Q.; Parastaev, A.; Chiang, F. K.; Longo, A.; Escudero, C.; Kosinov, N.; Hensen, E. J. M. Interface dynamics of Pd-CeO_2 single-atom catalysts during CO oxidation. *Nat. Catal.* **2021**, *4*, 469–478.

[5] Li, K. Z.; Haneda, M.; Ning, P. H.; Wang, H.; Ozawa, M. Microstructure and oxygen evolution of Fe-Ce mixed oxides by redox treatment. *Appl. Surf. Sci.* **2014**, *289*, 378–383.

[6] Li, M.; Pham, T. H. M.; Oveisi, E.; Ko, Y.; Luo, W.; Züttel, A. Revealing the surface chemistry for CO_2 hydrogenation on Cu/CeO_{2-x} using near-ambient-pressure X-ray photoelectron spectroscopy. *ACS Appl. Energy Mater.* **2021**, *4*, 12326–12335.

[7] Piotrowski, M. J.; Tereshchuk, P.; Da Silva, J. L. F. Theoretical investigation of small transition-metal clusters supported on the CeO_2(111) surface. *J. Phys. Chem. C* **2014**, *118*, 21438–21446.

[8] Lambrou, P. S.; Efstathiou, A. M. The effects of Fe on the oxygen storage and release properties of model Pd-Rh/CeO_2-Al_2O_3 three-way catalyst. *J. Catal.* **2006**, *240*, 182–193.

[9] Pham, C. N.; Van Trinh, Q.; Van Thai, D.; Dao, N. N.; Nguyen, B. Q.; Doan, D. T.; Le, H. B.; Van Nguyen, V.; Duong, L. T.; Tran, L. D. Synthesis of CeO_2-Fe_2O_3 mixed oxides for low-temperature carbon monoxide oxidation. *Adsorpt. Sci. Technol.* **2022**, *2022*, 5945169.

[10] Lei, Z. P.; Yan, J. C.; Fang, J.; Shui, H. F.; Ren, S. B.; Wang, Z. C.; Li, Z. K.; Kong, Y.; Kang, S. G. Catalytic combustion of coke and NO reduction *in-situ* under the action of Fe, Fe-CaO and Fe-CeO_2. *Energy* **2021**, *216*, 119246.

[11] Wu, X.; Qian, W. X.; Zhang, H. T.; Han, Z. H.; Zhang, H. W.; Ma, H. F.; Liu, D. H.; Sun, Q. W.; Ying, W. Y. Mn-decorated CeO_2 nanorod supported iron-based catalyst for high-temperature Fischer-Tropsch synthesis of light olefins. *Catal. Sci. Technol.* **2021**, *11*, 2577–2588.

[12] Li, H. C.; Li, K. Z.; Wang, H.; Zhu, X.; Wei, Y. G.; Yan, D. X.; Cheng, X. M.; Zhai, K. Soot combustion over $Ce_{1-x}Fe_xO_{2-\delta}$ and CeO_2/Fe_2O_3 catalysts: Roles of solid solution and interfacial interactions in the mixed oxides. *Appl. Surf. Sci.* **2016**, *390*, 513–525.

[13] Galvita, V.; Rihko-Struckmann, L. K.; Sundmacher, K. The CO adsorption on a Fe_2O_3-$Ce_{0.5}Zr_{0.5}O_2$ catalyst studied by TPD, isotope exchange and FTIR spectroscopy. *J. Mol. Catal. A: Chem.* **2008**, *283*, 43–51.

[14] Chen, H. T.; Chang, J. G. Computational investigation of CO adsorption and oxidation on iron-modified cerium oxide. *J. Phys. Chem. C* **2011**, *115*, 14745–14753.

[15] Tian, D.; Li, K. Z.; Wei, Y. G.; Zhu, X.; Zeng, C. H.; Cheng, X. M.; Zheng, Y. Z.; Wang, H. DFT insights into oxygen vacancy formation and CH_4 activation over CeO_2 surfaces modified by transition metals (Fe, Co and Ni). *Phys. Chem. Chem. Phys.* **2018**, *20*, 11912–11929.

[16] Lykaki, M.; Stefa, S.; Carabineiro, S. A. C.; Pandis, P. K.; Stathopoulos, V. N.; Konsolakis, M. Facet-dependent reactivity of Fe_2O_3/CeO_2 nanocomposites: Effect of ceria morphology on CO oxidation. *Catalysts* **2019**, *9*, 371.

[17] Ge, C. Y.; Yu, Y. X.; An, D. Q.; Tong, Q.; Tang, C. J.; Gao, F.; Sun, J. F.; Dong, L. Surface configuration modulation for FeO_x-CeO_2/γ-Al_2O_3 catalysts and its influence in CO oxidation. *J. Catal.* **2020**, *386*, 139–150.

[18] Cheng, X. W.; Tu, Y.; Zhang, D. L.; Huang, L. C.; Xu, Q.; Hu, J.; Cao, X.; Ding, H. H.; Han, D.; Ye, Y. F. et al. Unraveling the interaction between Fe and CeO_2(111) through growth, structure, and thermal stability studies. *J. Phys. Chem. C* **2024**, *128*, 11773–11783.

[19] Kong, D. D.; Wang, G. D.; Pan, Y. H.; Hu, S. W.; Hou, J. B.; Pan, H. B.; Campbell, C. T.; Zhu, J. F. Growth, structure, and stability of Ag on CeO_2(111): Synchrotron radiation photoemission studies. *J. Phys. Chem. C* **2011**, *115*, 6715–6725.

[20] Zhang, D. L.; Cao, X.; Tu, Y.; Cheng, X. W.; Huang, L. C.; Ding, H. H.; Hu, J.; Xu, Q.; Ye, Y. F.; Zhu, J. F. Unraveling the surface structure of ceria-supported bimetal Co-Cu nanoparticles. *J. Phys. Chem. C* **2024**, *128*, 9051–9059.

[21] Hu, S. W.; Wang, Y.; Wang, W. J.; Han, Y.; Fan, Q. T.; Feng, X. F.; Xu, Q.; Zhu, J. F. Ag nanoparticles on reducible CeO_2(111) thin films: Effect of thickness and stoichiometry of ceria. *J. Phys. Chem. C* **2015**, *119*, 3579–3588.

[22] Abbott, H. L.; Aumer, A.; Lei, Y.; Asokan, C.; Meyer, R. J.; Sterrer, M.; Shaikhutdinov, S.; Freund, H. J. CO adsorption on monometallic and bimetallic Au–Pd nanoparticles supported on oxide thin films. *J. Phys. Chem. C* **2010**, *114*, 17099–17104.

[23] Seip, U.; Tsai, M. C.; Christmann, K.; Küppers, J.; Ertl, G. Interaction of CO with an Fe(111) surface. *Surf. Sci.* **1984**, *139*, 29–42.

[24] Jiang, D. E.; Carter, E. A. Adsorption and dissociation of CO on Fe(110) from first principles. *Surf. Sci.* **2004**, *570*, 167–177.

[25] Cameron, S. D.; Dwyer, D. J. A study of. pi. -bonded carbon monoxide on iron(100). *Langmuir* **1988**, *4*, 282–288.
[26] Li, J. B.; He, X.; Peng, C.; Ahuja, R. Chemical bonding of unique CO on Fe(100). *J. Phys. Chem. C* **2018**, *122*, 9062–9074.
[27] Wang, T.; Tian, X. X.; Li, Y. W.; Wang, J. G.; Beller, M.; Jiao, H. J. Coverage-dependent CO adsorption and dissociation mechanisms on iron surfaces from DFT computations. *ACS Catal.* **2014**, *4*, 1991–2005.
[28] Wang, T.; Tian, X. X.; Li, Y. W.; Wang, J. G.; Beller, M.; Jiao, H. J. High coverage CO activation mechanisms on Fe(100) from computations. *J. Phys. Chem. C* **2014**, *118*, 1095–1101.
[29] Nassir, M. H.; Frühberger, B.; Dwyer, D. J. Coverage dependence of Co dissociation on clean and hydrogen presaturated Fe(100) surface. *Surf. Sci.* **1994**, *312*, 115–123.
[30] Lu, K.; He, Y. R.; Huo, C. F.; Guo, W. P.; Peng, Q.; Yang, Y.; Li, Y. W.; Wen, X. D. Developing ReaxFF to visit CO adsorption and dissociation on iron surfaces. *J. Phys. Chem. C* **2018**, *122*, 27582–27589.
[31] Oh, J.; Kondo, T.; Hatake, D.; Arakawa, K.; Suzuki, T.; Sekiba, D.; Nakamura, J. Adsorption of CO on iron clusters on graphite. *J. Phys. Chem. C* **2012**, *116*, 7741–7747.
[32] Graciani, J.; Mudiyanselage, K.; Xu, F.; Baber, A. E.; Evans, J.; Senanayake, S. D.; Stacchiola, D. J.; Liu, P.; Hrbek, J.; Fernández Sanz, J. et al. Highly active copper-ceria and copper-ceria-titania catalysts for methanol synthesis from CO_2. *Science* **2014**, *345*, 546–550.
[33] Vayssilov, G. N.; Mihaylov, M.; St. Petkov, P. ; Hadjiivanov, K. I.; Neyman, K. M. Reassignment of the vibrational spectra of carbonates, formates, and related surface species on ceria: A combined density functional and infrared spectroscopy investigation. *J. Phys. Chem. C* **2011**, *115*, 23435–23454.
[34] Moon, D. W.; Bernasek, S. L.; Lu, J. P.; Gland, J. L.; Dwyer, D. J. Activation of carbon monoxide on clean and sulfur modified Fe(100). *Surf. Sci.* **1987**, *184*, 90–108.
[35] Bartosch, C. E.; Whitman, L. J.; Ho, W. The adsorption, interconversion, and dissociation of CO on Fe(111). *J. Chem. Phys.* **1986**, *85*, 1052–1060.
[36] Wielers, A. F. H.; Kock, A. J. H. M.; Hop, C. E. C. A.; Geus, J. W.; van Der Kraan, A. M. The reduction behavior of silica-supported and alumina-supported iron catalysts: A mossbauer and infrared spectroscopic study. *J. Catal.* **1989**, *117*, 1–18.
[37] Benziger, J. B.; Larson, L. R. An infrared spectroscopy study of the adsorption of CO on Fe/MgO. *J. Catal.* **1982**, *77*, 550–553.
[38] Happel, M.; Mysliveček, J.; Johánek, V.; Dvořák, F.; Stetsovych, O.; Lykhach, Y.; Matolín, V.; Libuda, J. Adsorption sites, metal-support interactions, and oxygen spillover identified by vibrational spectroscopy of adsorbed CO: A model study on Pt/ceria catalysts. *J. Catal.* **2012**, *289*, 118–126.
[39] Couble, J.; Bianchi, D. Heats of adsorption of linear CO species adsorbed on reduced Fe/Al_2O_3 catalysts using the AEIR method in diffuse reflectance mode. *Appl. Catal. A: Gen.* **2011**, *409–410*, 28–38.
[40] Guglielminotti, E. Spectroscopic characterization of the Fe/ZrO_2 system: 1. *CO adsorption. J. Phys. Chem.* **1994**, *98*, 4884–4891.
[41] Zhao, J. Q.; Yang, Q.; Shi, R.; Waterhouse, G. I. N.; Zhang, X.; Wu, L. Z.; Tung, C. H.; Zhang, T. R. FeO-CeO_2 nanocomposites: An efficient and highly selective catalyst system for photothermal CO_2 reduction to CO. *NPG Asia Mater.* **2020**, *12*, 5.
[42] Benndorf, C.; Krüger, B.; Thieme, F. Unusually low stretching frequency for CO adsorbed on Fe(100). *Surf. Sci. Lett.* **1985**, *163*, L675–L680.
[43] Zhang, X. L.; Peng, Q. Q.; Chen, L.; Lu, Z. S.; Yang, Z. X.; Hermansson, K. A new Mars-van Krevelen mechanism for CO oxidation on a Ti-decorated MXene. *Adv. Mater. Interfaces* **2023**, *10*, 2300070.
[44] Rafaj, Z.; Krutel, J.; Nehasil, V. Oxygen exchange between catalyst and active support during CO oxidation on Rh/CeO_2(111) and Rh/CeO_2(110): Isotope labeled ^{18}O study. *J. Phys. Chem. C* **2021**, *125*, 15959–15966.
[45] Zhou, X.; Mannie, G. J. A.; Yin, J. Q.; Yu, X.; Weststrate, C. J.; Wen, X. D.; Wu, K.; Yang, Y.; Li, Y. W.; Niemantsverdriet, J. W. Iron carbidization on thin-film silica and silicon: A near-ambient-pressure X-ray photoelectron spectroscopy and scanning tunneling microscopy study. *ACS Catal.* **2018**, *8*, 7326–7333.
[46] Hunt, J.; Ferrari, A.; Lita, A.; Crosswhite, M.; Ashley, B.; Stiegman, A. E. Microwave-specific enhancement of the carbon-carbon dioxide (Boudouard) Reaction. *J. Phys. Chem. C* **2013**, *117*, 26871–26880.
[47] Grosvenor, A. P.; Kobe, B. A.; Biesinger, M. C.; McIntyre, N. S. Investigation of multiplet splitting of Fe 2p XPS spectra and bonding in iron compounds. *Surf. Interface Anal.* **2004**, *36*, 1564–1574.
[48] Droubay, T. C.; Chambers, S. A. Surface sensitive Fe *2p* photoemission spectra for α-Fe_2O_3 (0001)-The influence of symmetry and crystal-field strength. *Phys. Rev. B* **2001**, *64*, 205414.
[49] Gupta, R. P.; Sen, S. K. Calculation of multiplet structure of core *p*-vacancy levels. *II. Phys. Rev. B* **1975**, *12*, 15–19.
[50] Xu, Q.; Cheng, X. W.; Zhang, N. Q.; Tu, Y.; Wu, L. H.; Pan, H. B.; Hu, J.; Ding, H. H.; Zhu, J. F.; Li, Y. D. Unraveling the advantages of Pd/CeO_2 single-atom catalysts in the NO + CO reaction by model catalysts. *Nano Res.* **2023**, *16*, 8882–8892.
[51] Mudiyanselage, K.; Senanayake, S. D.; Feria, L.; Kundu, S.; Baber, A. E.; Graciani, J.; Vidal, A. B.; Agnoli, S.; Evans, J.; Chang, R. et al. Importance of the metal-oxide interface in catalysis: *In situ* studies of the water-gas shift reaction by ambient-pressure X-ray photoelectron spectroscopy. *Angew. Chem., Int. Ed.* **2013**, *52*, 5101–5105.
[52] Simonovis, J. P.; Zhang, H.; Rui, N.; Hunt, A.; Orozco, I.; Liu, P.; Senanayake, S. D.; Rodriguez, J. A.; Waluyo, I. Investigating the elusive nature of atomic O from CO_2 dissociation on Pd(111): The role of surface hydrogen. *J. Phys. Chem. C* **2022**, *126*, 7870–7879.
[53] Shipilin, M.; Degerman, D.; Lömker, P.; Goodwin, C. M.; Rodrigues, G. L. S.; Wagstaffe, M.; Gladh, J.; Wang, H. Y.; Stierle, A.; Schlueter, C. et al. *In situ* surface-sensitive investigation of multiple carbon phases on Fe(110) in the Fischer-Tropsch synthesis. *ACS Catal.* **2022**, *12*, 7609–7621.
[54] Jagannathan, K.; Srinivasan, A.; Hegde, M. S.; Rao, C. N. R. Interaction of carbon monoxide with transition metal surfaces. *Surf. Sci.* **1980**, *99*, 309–319.